Doppler Spectroscopy and Tomography of Plasmas

John HOWARD, Fenton GLASS[1)] and Clive MICHAEL[2)]

Plasma Research Laboratory, Australian National University, Canberra ACT 0200, Australia
[1)]*FOM-Institute for Plasma Physics, Rijnhuizen*
[2)]*National Institute for Fusion Science, Toki 509-5292, Japan*

(Received 12 December 2006 / Accepted 11 April 2007)

The interpretation of Doppler broadened spectral line shapes for extended radiating media, such as flames and discharges, is complicated by the spatial inhomogeneity of the source. In this paper, we consider the conditions under which the Doppler tomography problem is invertible. For media in drifting thermal equilibrium, it is found that the visibility of fringes produced by modulated or fixed-delay quadrature interferometers deliver the Radon transform of a quantity related to the inhomogeneous temperature distribution. In view of this, we introduce novel imaging polarization interferometers suitable for high spectral and temporal resolution plasma Doppler tomography. One such system has been used to obtain images of ion spectral-line brightness and temperature for low-field rf-heated argon discharges in the H-1NF heliac. Tomographic reconstructions for a number of different plasma régimes are presented.

Keywords: spectroscopy, tomography, coherence, polarization interferometry

DOI: 10.1585/pfr.2.S1014

1. Introduction

Doppler spectroscopy is a routine diagnostic for sensing the gross features of the velocity distribution of excited species in radiating, optically-thin media such as plasmas [1, 2]. Despite the simple linear mapping from velocity distribution to emission spectrum, interpretation is complicated by the fact that the Doppler shift conveys only the velocity component in the direction of view. For example, for a uniform medium in thermal equilibrium, and provided other line broadening mechanisms can be ignored, the spectral lineshape is a Gaussian whose width and shift are related respectively to the temperature and the component of the gross motion (for example, rotation) of the emitting species in the direction of view. When the distribution function $f(\boldsymbol{r}, \boldsymbol{v})$ is inhomogeneous, the measured spectrum is the local intensity-weighted summation of Gaussians of varying width and shift. The problem thus combines the 3-d Radon transform of the velocity distribution function (integration over planes) brought about by the Doppler effect and the 2-d Radon transform (integration over lines) of the spatially inhomogeneous radiating source. Even when measurements can be made along many viewing lines, the inverse problem remains ill-posed.

A mathematical outline of the problem and an overview of time-domain spectroscopic techniques are presented in Section 2. A reciprocal space description of the Doppler tomography problem is developed in Section 3 and conditions under which the problem can be inverted are identified. Given the special relationship between tomography and reciprocal space, it is not surprising that simple relationships are also found to link the output of a fixed delay Fourier transform spectrometer (the complex degree of coherence) and the line-integrals of scalar and vector fields that characterize the inhomogeneous radiating source. For the case of drifting local thermal equilibrium, tomographic measurements (i.e. line-integrated measurements at all angles and impact parameters) of the light coherence at a single fixed delay suffice for the reconstruction of the emission intensity (dc), flow vorticity (phase) and species temperature (fringe visibility).

Motivated by these theoretical insights, we have developed single and multiple fixed-delay, modulatable and static polarization interferometers for various emission spectroscopy applications. Modulatable optical delays can be introduced using solid birefringent and electro-optic crystals [3]. These interferometric systems can be adapted easily for two-dimensional imaging applications where detecting elements in the image plane capture independent line-integrated spectroscopic images by electro-optically stepping the interferometric phase synchronously with the camera frame rate [4]. Static systems can also be configured for 2-D coherence imaging by multiplexing quadrature interferometric phase images to the quadrants of a CCD camera [5]. Though the focus is on applications involving extended sources, these instruments are also suited to localized measurements such as charge exchange recombination Doppler spectroscopy and motional Stark effect in particle beam-heated plasmas. [6, 7].

To conclude this paper we present images of ion spectral-line emission intensity and temperature for a number of different confinement regimes that have been tomo-

author's e-mail: john.howard@anu.edu.au

graphically inverted without recourse to imposed assumptions or constraints.

2. Doppler Spectroscopy

We consider transition radiation (centre frequency ν_0) from an optically thin inhomogeneous medium. In terms of the normalized frequency coordinate $\xi = (\nu - \nu_0)/\nu_0$, the normalized spectral lineshape $g(\boldsymbol{r}, \xi; \hat{\boldsymbol{l}})$ of light emitted from some position $\boldsymbol{r} = (x, y)$ in the medium, and in direction $\hat{\boldsymbol{l}} = (-\sin\theta, \cos\theta)$ is assumed to be determined predominantly by the Doppler effect:

$$g(\boldsymbol{r}, \xi; \hat{\boldsymbol{l}}) = \int f(\boldsymbol{r}, \boldsymbol{v})\, \delta(\xi - \boldsymbol{v}.\hat{\boldsymbol{l}})\, \mathrm{d}\boldsymbol{v}. \tag{1}$$

The delta function selects those particles in the velocity distribution of the radiating species $f(\boldsymbol{r}, \boldsymbol{v})$, where $\boldsymbol{v} = \boldsymbol{V}/c$ and $\boldsymbol{V} = (V_x, V_y, V_z)$ is the species velocity vector, having velocity component $\boldsymbol{v}.\hat{\boldsymbol{l}}$ giving rise to emission frequency ξ. The spectrum g thus gives integrals of the 3D velocity distribution function f over the set of planes perpendicular to $\hat{\boldsymbol{l}}$ and distant ξ from the origin as shown in Fig. 1. Since the viewing line is assumed to lie in the x-y plane, it is sufficient to regard f as a function of v_x and v_y only. It is convenient to introduce the spectrally integrated intensity $I_0(\boldsymbol{r})$ such that $f = I_0 \hat{f}$ where $\hat{f}$ is the probability density function associated with f.

Assuming the radiated intensity is isotropic, the measured emission spectrum can be approximated by an integral $e(\xi; \hat{\boldsymbol{l}})$ of the intensity weighted spectrum along the line $L(p, \theta)$ with impact parameter p and angle θ (direction $\hat{\boldsymbol{p}} = (\cos\theta, \sin\theta)$ orthogonal to $\hat{\boldsymbol{l}}$) in the observation cross-section (see Fig. 2):

$$\begin{aligned} e(\xi; \hat{\boldsymbol{l}}) &= \int g(\boldsymbol{r}, \xi; \hat{\boldsymbol{l}})\, \delta(p - \boldsymbol{r}.\hat{\boldsymbol{p}})\, \mathrm{d}\boldsymbol{r} \\ &\equiv \int_L g(\boldsymbol{r}, \xi; \hat{\boldsymbol{l}})\, \mathrm{d}l. \end{aligned} \tag{2}$$

We refer to the collection of all line integrals in a given direction $\hat{\boldsymbol{p}}$ as a view or projection. For notational simplicity we do not explicitly label line integral quantities, but retain reference to the direction $\hat{\boldsymbol{l}}$ where appropriate. The shape of the spectral line is an intensity weighted mixture of contributions from all parts of the emitting volume along the line of sight, each characterized by possibly distinct probability density functions.

The inverse problem, namely to infer the properties of the species velocity distribution function $f(x, y, v_x, v_y)$ from measurements of the spectral line profile for all p, ξ and θ is clearly ill-posed. With *a priori* assumptions (e.g. radial symmetry, isotropy, Maxwellian distributions etc.), however, it is possible to infer certain properties of the velocity distribution from the line-integrated spectral profile (see, for example, [8]).

2.1 Temporal coherence

The degree to which various simplifying assumptions

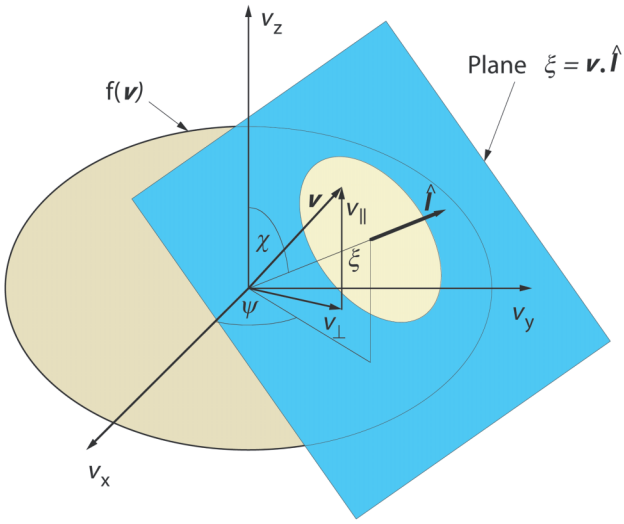

Fig. 1 The planar projection (Radon transform) of the 3D velocity distribution function is the surface integral of f over the plane $\xi = \boldsymbol{v}.\hat{\boldsymbol{l}}$. The ellipsoid represents an iso-surface of the velocity distribution function f.

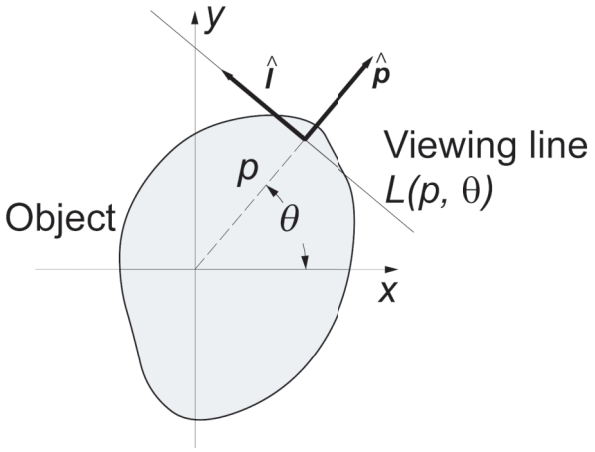

Fig. 2 Geometry for tomography of some 2-d scalar object O showing the relationship between unit vector $\hat{\boldsymbol{l}}$ and the viewing line $L(p, \theta)$ at impact parameter and angle θ.

are either necessary or helpful is revealed by the reciprocal space properties of the emission spectrum $e(\xi; \hat{\boldsymbol{l}})$. This leads to a consideration of the Fourier transform spectrometer which measures the temporal coherence of the emission line.

For quasi-monochromatic radiation, a given polarization component of the ideal line-integrated field u can be expressed as the analytic signal

$$u(t; \hat{\boldsymbol{l}}) = A(t; \hat{\boldsymbol{l}}) \exp(-\mathrm{i}2\pi\nu_0 t) \tag{3}$$

where the complex amplitude A changes slowly compared with the exponential and ν_0 is the light centre frequency [9]. The Fourier transform spectrometer (interferometer) splits the wave, relatively delaying the nominally equal amplitude components by time τ before they are recom-

bined at a square-law detector. In terms of the corresponding phase delay $\phi = 2\pi\nu_0\tau$, the intensity of the transmitted or reflected light at the final beam combiner, can be expressed as

$$S_{\pm}(\phi) = \frac{\mu_0}{2}\Big[1 \pm \Re[\gamma(\hat{\phi};\hat{\boldsymbol{l}})\exp(\mathrm{i}\phi)]\Big] \tag{4}$$

where $\mu_0 = \langle u\,u^*\rangle$ is the line integral of the spectrally integrated intensity $I_0(\boldsymbol{r})$ and $\gamma(\hat{\phi};\hat{\boldsymbol{l}})$ is the temporal-coherence of the spectral line. Note that γ is a function of the group phase delay coordinate $\hat{\phi} = \kappa\phi$, where

$$\kappa = 1 + \frac{\nu_0}{\tau_0}\frac{\partial\tau}{\partial\nu}\,|_{\nu_0} \tag{5}$$

accounts for any optical frequency dispersion of the time delay.

For stationary processes, the temporal coherence is related to the emission spectral distribution through the Weiner-Khinchine theorem [10]

$$\gamma(\phi;\hat{\boldsymbol{l}}) = \frac{1}{\mu_0}\int_{-\infty}^{\infty} e(\xi;\hat{\boldsymbol{l}})\,\exp(\mathrm{i}\phi\xi)\,\mathrm{d}\xi. \tag{6}$$

Substituting from Eq. (1) we obtain

$$\gamma(\phi;\hat{\boldsymbol{l}}) = \frac{1}{\mu_0}\int_L G(\boldsymbol{r},\phi\hat{\boldsymbol{l}})\,\mathrm{d}l \tag{7}$$

where

$$G(\boldsymbol{r},\phi\hat{\boldsymbol{l}}) \equiv \mathcal{F}[g(\boldsymbol{r},\xi;\hat{\boldsymbol{l}})] \tag{8}$$

$$= \int f(\boldsymbol{r},\boldsymbol{v})\,\exp(\mathrm{i}\phi\boldsymbol{v}.\hat{\boldsymbol{l}})\,\mathrm{d}\boldsymbol{v}. \tag{9}$$

Writing $G(\boldsymbol{r},0) = I_0(\boldsymbol{r})\hat{G}(\boldsymbol{r},\phi\hat{\boldsymbol{l}})$, we note that $\hat{G}(\boldsymbol{r},0) = 1$ and hence $\gamma(0;\hat{\boldsymbol{l}}) = 1$. For convenience, we refer to G as the "Doppler-coherence" transform of the distribution function f.

3. Doppler Tomography

According to Eq. (9), the Doppler coherence transform gives a one-dimensional central slice of the two dimensional Fourier transform of the distribution function along the phase delay vector $\boldsymbol{\phi} = \phi\hat{\boldsymbol{l}}$

$$F(\boldsymbol{r},\boldsymbol{\phi}) = \int f(\boldsymbol{r},\boldsymbol{v})\,\exp(\mathrm{i}\boldsymbol{\phi}.\boldsymbol{v})\,\mathrm{d}\boldsymbol{v}. \tag{10}$$

This is a restatement of the projection theorem of reconstructive tomography following from the Radon transform expressed by Eq. (1).

If we Fourier transform the emission spectrum $e(\xi;\hat{\boldsymbol{l}})$ given by Eq. (2) over both impact parameter p and normalized frequency ξ we obtain a projection theorem for the full 2-d Doppler tomography problem:

$$E(k,\phi;\hat{\boldsymbol{l}}) = F(k\hat{\boldsymbol{p}},\phi\hat{\boldsymbol{l}}). \tag{11}$$

Because the directions $\hat{\boldsymbol{l}}$ and $\hat{\boldsymbol{p}}$ cannot be chosen independently, it is, in general, impossible to recover the four-dimensional function $\hat{f}(x,y,v_x,v_y)$ from the three dimensional data $E(k,\phi;\hat{\boldsymbol{l}})$. However, if $\hat{f}(\boldsymbol{r},\boldsymbol{v})$ is spatially circularly symmetric (and so independent of the view direction), it should be possible to recover the arbitrary velocity distribution function $f(r,\boldsymbol{v})$ from measurements covering the space (ϕ,θ). Conversely, and more usefully, if $f(\boldsymbol{r},\boldsymbol{v})$ is isotropic in velocity space, it should be possible to fully reconstruct the associated distribution function $\hat{f}(\boldsymbol{r},v)$ from measurements filling the space (k,θ).

3.1 Drifting isotropic distribution

On translating to the coordinate system drifting with local mean velocity $\boldsymbol{v}_D(\boldsymbol{r})$, the Doppler-coherence transform assumes the simple form

$$G(\boldsymbol{r},\phi\hat{\boldsymbol{l}}) = \exp(\mathrm{i}\phi\boldsymbol{v}_D.\hat{\boldsymbol{l}})G_0(\boldsymbol{r},\phi\hat{\boldsymbol{l}}) \tag{12}$$

where $G_0(\boldsymbol{r},\phi\hat{\boldsymbol{l}}) = F_0(\boldsymbol{r},\phi\hat{\boldsymbol{l}})$ and $F_0 = \mathcal{F}f_0$ is the Fourier transform of the centered distribution f_0. Note that the modulus of the complex coherence (the interferometer fringe visibility, or contrast) which characterises the inhomogeneous distribution, is insensitive to the drift $\boldsymbol{v}_D$:

$$|\gamma(\phi;\hat{\boldsymbol{l}})| = \frac{1}{\mu_0}\int_L |G_0(\boldsymbol{r},\phi\hat{\boldsymbol{l}})|\;\mathrm{d}l. \tag{13}$$

The inverse Fourier transform of the fringe visibility is the same as the signal that would be yielded directly by a grating spectrometer with narrow slits and provided the drift component $\boldsymbol{v}_D = 0$.

When f_0 is isotropic, G_0 is real and even and independent of the view direction $\hat{\boldsymbol{l}}$. Provided also that $\phi\boldsymbol{v}_D$ is small, a quantity related to the vector flow field can be obtained from the imaginary part of $\gamma = \gamma_c + \mathrm{i}\gamma_q$:

$$\gamma_q = \phi\frac{1}{\mu_0}\int_L G_0(\boldsymbol{r},\phi)\,\boldsymbol{v}_D.\mathrm{d}\boldsymbol{l}. \tag{14}$$

The phase offset ϕ can be chosen to magnify the usually small Doppler shift component but not so large as to invalidate the first order approximation leading to Eq. (14). In response to small variations in the local drift speed $\boldsymbol{v}_D$, the interferogram phase varies (much like an accordion), leaving the fringe visibility unchanged. This is a consequence of the Fourier shift theorem. On the other hand, when the shape of the locally symmetric distribution f_0 changes (but not its first moment), only the fringe visibility is affected, the underlying phase remaining undisturbed. This decoupling of the shift and shape is one of the more important advantages offered by time-domain spectroscopic methods applied to Doppler tomography.

As already noted, for an isotropic distribution function, the fringe visibility $|\gamma|$ is independent of the viewing direction $\hat{\boldsymbol{l}}$ and independent of the spatially varying drift $\boldsymbol{v}_D$. As a result, complete measurements of an inhomogeneous source at points (p,θ) covering the projection space and at all delays φ are sufficient to fully reconstruct the isotropic distribution function.

3.2 Local thermal equilibrium

When G_0 can be characterized by a single parameter (such as temperature in the case of thermal equilibrium), tomographic measurements at only a single phase delay offset are sufficient to recover the spatial distribution of the parameter. When the radiating medium is in drifting LTE, the normalized distribution function is given by

$$\hat{f}_0(\boldsymbol{r}, v) = (\pi {v_{\rm th}}^2)^{-3/2} \exp(-v^2/{v_{\rm th}}^2) \qquad (15)$$

where $v_{\rm th}(\boldsymbol{r})$ is related to temperature. The local emission spectrum in the direction $\hat{\boldsymbol{l}}$ is obtained on substitution into Eq. (1) as

$$\hat{g}_0(\boldsymbol{r}, \xi) = (\pi {v_{\rm th}}^2)^{-1/2} \exp[-(\xi - \boldsymbol{v}_D.\hat{\boldsymbol{l}})^2/{v_{\rm th}}^2]. \qquad (16)$$

Since the exponent involves $\boldsymbol{r}$ dependent unknowns $\boldsymbol{v}_D.\hat{\boldsymbol{l}}$ and $v_{\rm th}$, and because the measurement convolves $\hat{g}_0(\boldsymbol{r}, \xi)$ with the instrument spectral response, the tomography of $e(\xi; \hat{\boldsymbol{l}})$ presents a difficult inverse problem.

The modulus of the local Doppler-coherence transform, on the other hand, assumes a particularly simple form

$$\hat{G}_M(\phi) = \exp(-\phi^2 {v_{\rm th}}^2/4) \qquad (17)$$

where subscript M indicates a Maxwellian distribution and $G_M = I_0 \hat{G}_M$. In terms of the local species temperature $T_S(\boldsymbol{r})$, we write this as

$$\hat{G}_M(\boldsymbol{r}, \phi) = \exp[-T_S(\boldsymbol{r})/T_C] \qquad (18)$$

with

$$kT_C = \frac{1}{2} m_S V_C^2 \qquad V_C = \frac{2c}{\phi} \qquad (19)$$

where T_C is a "characteristic temperature" set by the interferometer phase delay ϕ and V_C is the corresponding "characteristic velocity".

By making separate measurements at distinct (preferably quadrature) delay offsets ϕ, it is apparent from Eqs. (4), (14) and (18) that the signals from a modulated, single fixed-delay interferometer can be related directly to line integral measurements of the scalar field $G_0 = I_0 \hat{G}_0$ and longitudinal line integral measurements of the vector field $G_0 \boldsymbol{v}_D$. Tomographic reconstructions of simulated vector flow fields in the case of drifting thermal equilibrium have been presented elsewhere [11].

4. Multi-View Spectroscopic Doppler Tomography System

Projections of Doppler-broadened argon ion emission (488 nm) in low-field radio-frequency-heated (rf) discharges in the H-1NF heliac have been obtained using arrays of lens-coupled optical fibres that encircle the plasma poloidal cross-section [12]. The collected light is transmitted to a coherence imaging camera [13] which processes the spectral information to produce line-integrated estimates of the brightness, brightness-weighted plasma temperature and flow fields.

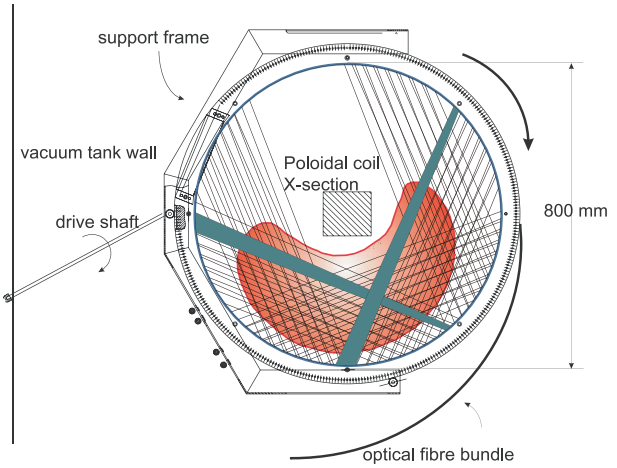

Fig. 3 Schematic diagram of the in-vacuum light-collection system—consisting of five viewing modules, with eleven lens-coupled optical fibres each, mounted on a rotatable carrier ring—encircling the plasma region. The solid stripes show projections of typical viewing cones.

The light-collection system consists of five identical modules each housing eleven parallel lens-coupled optical fibres. The modules, are mounted at intervals of 45° on the rim of a rotatable carrier ring which poloidally encircles the plasma . The carrier ring and supporting C-frame reside inside the vacuum tank. During rotation the optical fibres are spooled onto the ring circumference, allowing the viewing modules to be moved by up to 200°. For sufficiently reproducible plasmas, the ring can be rotated, on a shot-to-shot basis, to a number of distinct viewing stations to improve the sampling of the sinogram. Figure 3 is a schematic of the light-collection system installed between the toroidal field coils. A full description of the optical system and its characterization is presented elsewhere [14].

Large core (1mm) silica fibres transmit the light to a coherence-imaging spectrometer, which is external to the vacuum tank. This spectrometer is a field-widened imaging polarization interferometer that utilizes an electro-optic, birefringent crystal modulated about a fixed optical delay to resolve the complex coherence of the spectrally isolated 488 nm emission line. The modulation amplitude is approximately 0.8π and the frequency is 50 kHz. The interference fringes are imaged onto an 8×8 multi-anode photomultiplier array, allowing time resolved estimates of the ion flow and temperature using a single detector per line-of-sight channel. The results presented in this paper are restricted to reconstructions of the measured brightness and the ion temperature. Figure 4 shows the optical layout of the coherence imaging optical system used with the 55-channel tomographic spectroscopy system. Instrumental details are given in [15].

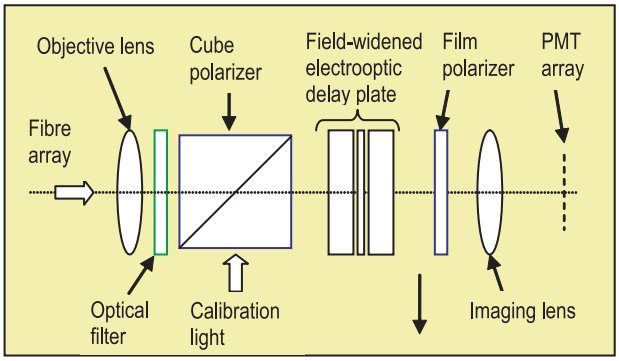

Fig. 4 Optical layout for modulated, field-widened imaging polarization interferometer used with the 55-channel tomographic spectroscopy system on H-1NF.

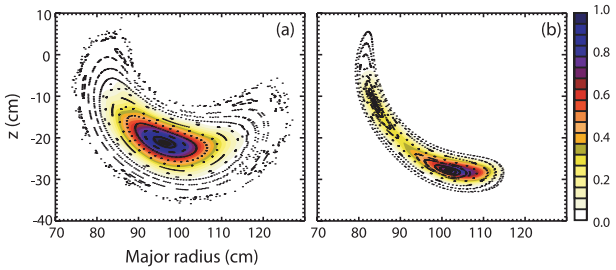

Fig. 5 Tomographic reconstructions of argon ion spectral-line brightness for (a) low field (.043 T) standard magnetic configuration, (b) birfurcated configuration near rotational transform of 0.5 per field period. Poincaré plots of the calculated magnetic flux surfaces at the toroidal position of the light collection system are shown superimposed on the reconstructions. The effects of the coherent mode structure have been removed by averaging over an oscillation period.

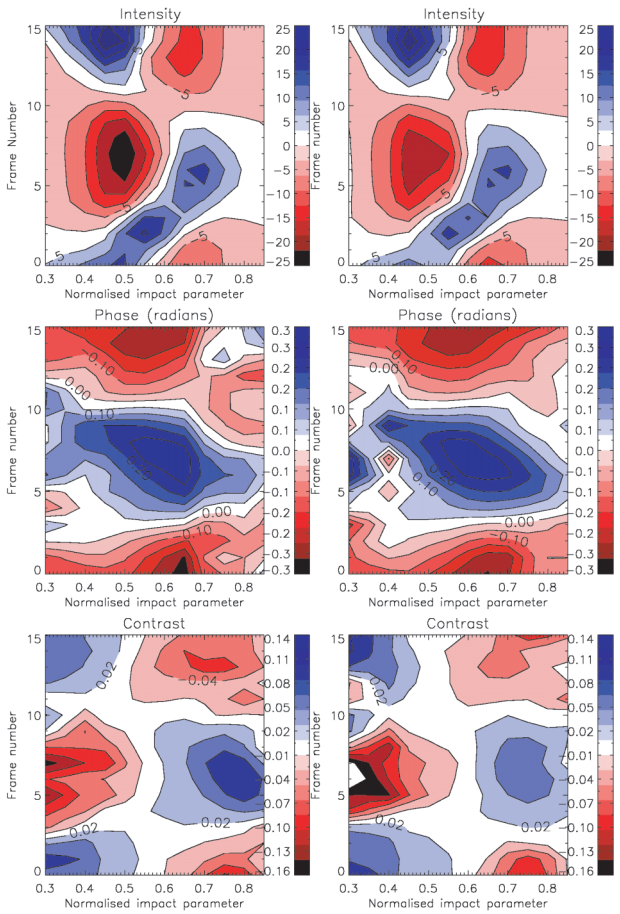

Fig. 6 From top to bottom: Contours of projections of brightness, phase shift and contrast for one cycle of the coherent instability. There are 16 time samples per period of the oscillation (vertical axis). The projections are measured using Module 3 at 0° wheel rotation (left column) and Module 4 at 45° wheel rotation (right column). There is good agreement between the two data sets which should be identical.

The entire system requires careful calibration to determine, for each channel, the spatial response in the plasma region, the interferometer instrument function, the relative channel sensitivity and the effects of cross-talk in the detector and optical system. These quantities are determined using miniature fluorescent tubes mounted inside the vacuum within the field of view of the rotating ring, and, for the interferometer, a monochromatic light source at or near the wavelength of the selected spectral line.

4.1 Plasma results

The H-1NF heliac has three field periods and can access a wide range of magnetic configurations [16]. By altering the ratio of the currents in the various control coils and the main toroidal field coil set, the rotational transform can be varied between $\sim$1.0-2.0 and the poloidal cross-sectional shape can be changed significantly.

Figure 5(a) shows the reconstructed brightness for the 'standard' magnetic field configuration (no current in the helical control winding, on-axis transform $\approx$ 1.1) for an on-axis field strength of 0.043 T. Fig. 5(b) shows brightness contours for a bifurcated field configuration having rotational transform near 0.5 per field period and field strength of 0.11 T. This atypical configuration was deliberately chosen to test the system imaging capability. Poincaré plots of the computed magnetic flux surfaces at the position of the light-collection system are shown superimposed over the brightness reconstructions.

For all reconstructions, data obtained at different viewing stations for nominally identical discharges are normalized in brightness using signals from a fixed-view coherence-imaging camera. Given the relatively dense sampling of the sinogram—a total of 344 line-integrated measurements for Fig. 5(a) and 500 for Fig. 5(c)—an iterative arithmetic reconstruction technique (ART) was sufficient to obtain consistent and reliable reconstructions. In both cases, the reconstructions conform closely with the computed flux surfaces.

Under certain discharge conditions in standard con-

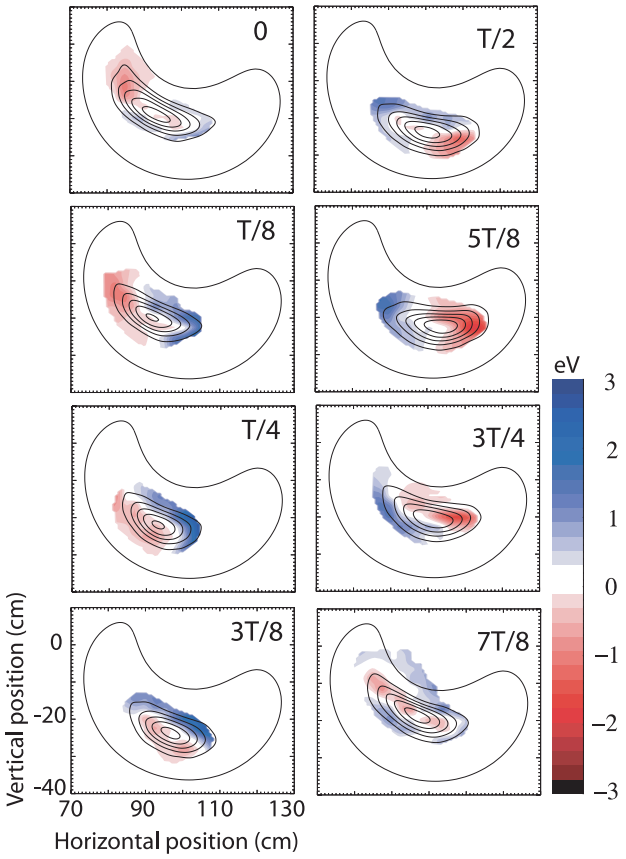

Fig. 7 Overlaid reconstructions of argon ion spectral-line brightness (contours) and temperature (false colour) at equispaced phases during an unstable low-field (0.043 T) plasma discharge in standard magnetic configuration.

figuration, a global coherent instability can be observed (fill pressure $\sim 3 \times 10^{-5}$ torr, rf heating power 60 kW, on-axis magnetic field strengths 0.043-0.13 T). This mode is sufficiently reproducible to allow consistent measurements to be obtained at a number of independent observing stations (wheel locations). The light signals are averaged over many oscillation periods with magnetic pickup coil signals used to synchronize independent data sets and to track small drifts in mode frequency. Projections of the brightness, phase shift and contrast throughout one cycle of the instability in nominally equivalent view directions (i.e. the ring is rotated 45° to bring adjacent modules into coincidence) are shown in Fig. 6, with each column representing a viewing station. These data are inverted using a minimum Fisher algorithm for both equilibrium and fluctuating quantities but with no assumptions regarding the spatial structure of the mode or its rotation.

Figure 7 shows the overlaid reconstructions of the total brightness and temperature fluctuation at equispaced phases of the mode rotation (period T ≈ 0.32 ms). Note that Fig. 5(a) shows the dc component of the brightness associated with this discharge. The amplitude of the brightness and temperature fluctuations are comparable with the corresponding cycle-averaged quantities. The reconstructed cycle-averaged ion temperature profile is found to be slightly hollow, in agreement with 1-D reconstructions based on flux-surface symmetry presented elsewhere [13, 17]. More details on the reconstruction technique and the nature of the oscillation are found in [14].

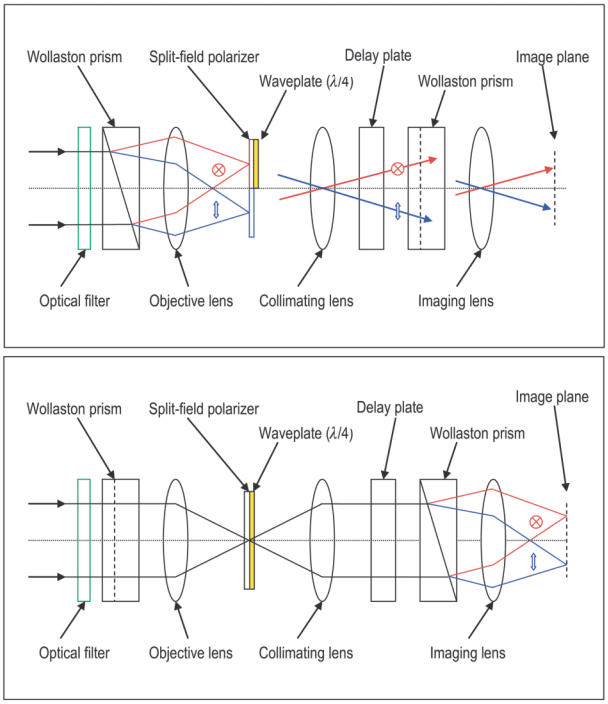

Fig. 8 Schematic view of optical layout for producing 4-quadrant coherence images of a quasi-monochromatic source. See text for discussion. (Reproduced from [5])

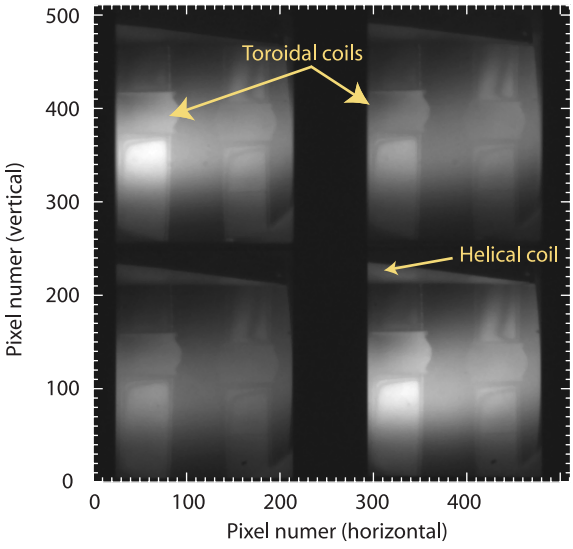

Fig. 9 Raw 4-quadrant 512 × 512 image. The individual images are inverted. (Reproduced from [5])

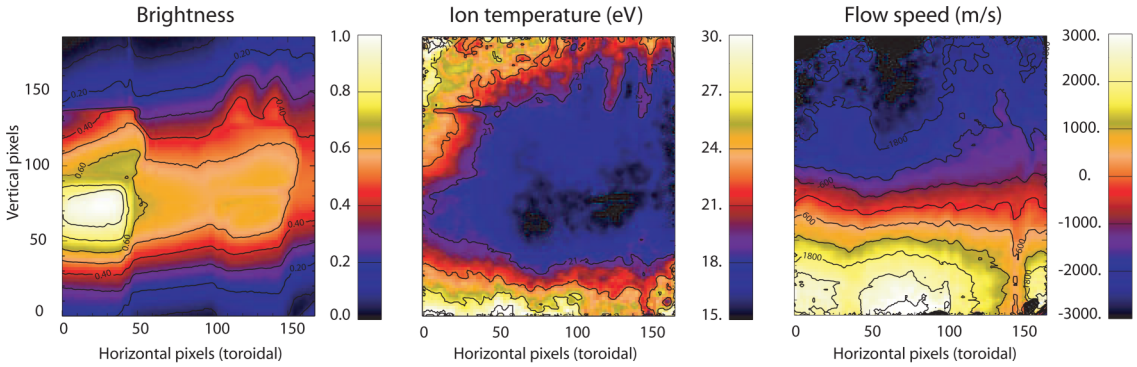

Fig. 10 Reduced 4 quadrant image showing average brightness, ion temperature and flow fields - see text for discussion. (Reproduced from [5])

5. Quadrant Coherence Imaging

The quadrant coherence imaging (QCI) system is a static polarization interferometer that multiplexes independent images of the optical coherence to the four corners of an imaging CCD array or other imaging detector [5]. A spatial multiplex approach (no modulation) allows snapshot imaging of fast transient events (e.g. combustions) or synchronous imaging of reproducible phenomena. The optical system is, in-principle, 100% light efficient while the use of passive components allows straightforward extension to the ultraviolet spectral region (> 200 nm). Hybrid spatio-temporal multiplex systems can be constructed for the study of more complex spectral scenes when more than four parameters are required for their description.

Figure 8 shows the optical layout of the QCI system in elevation and plan. The front end Wollaston and lens produce dual orthogonally polarized images of the source. A split-polarizer at the image plane isolates the images and a quarter waveplate produces a 90° phase shift in one image. These beams are angularly multiplexed through the fixed-delay polarization interferometer and a final Wollaston produces antiphase interferograms for each of the source images. The four images generate a quadrature sampling of the interferogram about a fixed delay set by the delay plate.

Figure 9 shows a typical camera plasma snapshot in the H-1NF heliac. Visible in each quadrant, illuminated by the plasma ion light, are two of the 36 internal toroidal field coils (TFCs) and their clamps. At the top of each image is the outline of the helical conductor. Each of the images is inverted so that the plasma actually resides above this conductor and is enclosed by the TFCs. Notice the presence of strong specular reflections from the leftmost of the TFCs in the image.

The extracted brightness, temperature and flow speed images for an argon discharge at 0.12 T in standard magnetic configuration and for a 30 mm lithium niobate delay plate (T_c = 24 eV) are shown in Fig. 10. A 5-pixel median filter has been applied to the temperature and flow images. The ion temperature profile is substantially hollow while the flow approximates rigid rotation. Observe that the brightness, temperature and flow images show little evidence of cross-coupling. Residual registration inaccuracies, which are evident in the flow and temperature images are likely due to spherical distortions produced by the first simple negative lens, and which are not corrected by our simple shifting algorithm. Observe that the temperature image is artificially elevated in high flow regions where light is also received by reflection from the coil surface. This is likely the result of the superposition of both blue and red shifted light resulting in a decrease in fringe contrast.

Acknowledgements

The authors wish to thank Dr Boyd Blackwell for assistance with H-1 machine operations and for useful discussions of the data and results.

[1] D. Rees and A. Greenaway, Appl. Opt. **22**, 1078 (1983).
[2] R. Bell *et al.*, Rev. Sci. Instrum. **70**, 821 (1999).
[3] J. Howard, Rev. Sci. Instrum. **70**, 368 (1999).
[4] J. Chung, R. Konig, T. Klinger and J. Howard, Plasma Phys. Control. Fusion **47**, 919 (2005).
[5] J. Howard, Rev. Sci. Instrum **77**, 10F111 (2006).
[6] F.M. Levinton *et al.*, Phys. Rev. Lett. **63**, 2060 (1989).
[7] J. Howard, Plasma Phys. Control. Fusion **41**, 271 (1999).
[8] R.S. Shaw, J. Opt. Soc. Am. A **4**, 2254 (1987).
[9] J. Goodman, *Statistical Optics* (John Wiley and Sons, New York, 1985).
[10] M. Born and E. Wolf, *Principles of Optics* (Pergamon Press, Oxford, 1980).
[11] J. Howard, Plasma Phys. Control. Fusion **38**, 489 (1996).
[12] F. Glass, Ph.D. thesis, Australian National University, 2004.
[13] J. Howard, C. Michael, F. Glass and A. Cheetham, Rev. Sci. Instrum. **72**, 888 (2001).
[14] F. Glass and J. Howard, In preparation (2007).
[15] J. Howard, Appl. Opt. **41**, 197 (2002).
[16] S. Hamberger, B. Blackwell, L. Sharp and D. Shenton, Fusion Technology **17**, 123 (1990).
[17] C. Michael, J. Howard and B. Blackwell, Phys. Plasmas **11**, 4008 (2004).